Available online at www.sciencedirect.com

ScienceDirect

journal homepage: http://www.elsevier.com/locate/acme

Original Research Article

Instabilities in membrane tension: Parametric study for large strain thermoplasticity

Marzena Mucha [a,*], *Balbina Wcisło* [a], *Jerzy Pamin* [a], *Katarzyna Kowalczyk-Gajewska* [b]

[a] *Institute for Computational Civil Engineering, Cracow University of Technology, Cracow, Poland*
[b] *Institute of Fundamental Technological Research, Polish Academy of Science, Warsaw, Poland*

ARTICLE INFO

Article history:
Received 21 August 2017
Accepted 10 December 2017
Available online 18 March 2018

Keywords:
Thermoplasticity
Large strains
Strain localization
Parametric study

ABSTRACT

This paper deals with the numerical analysis of localized deformation for a rectangular plate in membrane tension, modelled with large strain thermoplasticity. The aim is to determine the influence of selected factors on the localization phenomena, which can result from geometrical, material, and thermal softening. Two types of boundary conditions are considered: plane stress and plane strain, as well as two yield functions, Huber–Mises–Hencky and Burzyński–Drucker–Prager, with selected values of friction angle. First, isothermal conditions are considered and next, a conductive case with thermal softening is studied. Moreover, three types of plastic behaviour are analysed: strain hardening (with different values of hardening modulus), ideal plasticity, and strain softening. Numerical tests, performed using AceGen/FEM packages, are carried out for the rectangular plate under tension with an imperfection, using three finite element discretizations. The results for plane strain in the isothermal model show that with the decrease of linear hardening modulus, we can observe stronger mesh sensitivity, while for plane stress, mesh sensitivity is visible for all cases. Furthermore, for the thermomechanical model the results also depend on the mesh density due to insufficient heat conduction regularization.

1. Introduction

Tension in a membrane structure made of an elastoplastic material can lead to localized deformation which, depending on the adopted parameters and conditions, can take a form of a shear band or a neck. The former is referred to as a localized mode, whereas the latter is a diffuse one [4]. Such localization can have three sources: material (e.g. degradation of stiffness in a damage process or plasticity with softening), thermal (influence of temperature on material parameters), and geometrical (due to large deformations). In contrast to the first two sources, the last one is considered at the level of a specimen (not at the material point) and occurs when a cross-section of the elongated sample decreases while stresses are limited by the yield condition [16].

Localization phenomena are related to the notion of instability which was extensively studied for isothermal cases

* *Corresponding author.*
E-mail address: mmucha@L5.pk.edu.pl (M. Mucha).
https://doi.org/10.1016/j.acme.2018.01.008

by for example [8,19,25,5] or [17]. The theoretical analysis of sheet necking is included in [23]. When thermo-mechanical coupling is taken into account, the analysis of the localization phenomena is much more complicated. Usually, the increase of temperature causes thermal softening manifest itself in the degradation of the elastic stiffness and/or reduction of the yield strength. However, at the same time, conductivity can have a regularizing effect and influences the width of the occurring shear bands. Theoretical or numerical aspects of the unstable behaviour of materials in thermomechanical context can be found, for instance, in [12,2,3]. In the recent paper [27], a thermoplastic material model with the Huber–Mises–Hencky yield criterion is also considered and special attention is paid to the regularization of strain localization, resulting from heat conduction and/or a gradient enhancement related to the temperature field. In particular, two modes of localization are simulated: necking in an elongated circular bar and shear banding in a tensioned rectangular plate in plane strain conditions. The numerical tests, whose results are presented in the aforementioned paper, are carried out for different values of the heat conduction coefficient and internal length scale.

In this paper, attention is focused on local material models. The analysis of shear banding for a tensioned rectangular plate simulated with gradient-enhanced plasticity can be found in [15], whereas the coupled thermomechanical response of gradient plasticity is approached in [1].

To the author's knowledge, there is a scarcity of comprehensive parametric study on the localization phenomena for large strain (thermo-)elasto-plasticity. Thus, the aim of this paper is to numerically investigate the influence of selected factors on the localised deformation. The analysed benchmark is a rectangular plate under tension with an imperfection in the center. The specimen is modelled using three dimensional elasto-plastic finite elements and, depending on the applied boundary conditions, plane strain or plane stress state is obtained. The analysis is performed for two yield criteria: Huber–Mises–Hencky and Burzyński–Drucker–Prager. Additionally three types of plastic behaviour are taken into account: softening, hardening, or ideal plasticity. The analysis is firstly performed for the isothermal case, and next the full thermomechanical coupling is approached, which involves thermal expansion, thermal softening, and plastic dissipation as the source of material heating. Different values of the coefficient of thermal conductivity are tested. Basic assumptions and limitations utilized in the work are as follows: initial isotropy of the material model, rate-independent plasticity with associative flow rule, static loading, and, for thermo-mechanical coupling, transient heat flow with the Fourier law. From the computational point of view, an ill-posed problem, which is related to the localization phenomenon, leads to discretization-dependent results: the width of a localization zone is governed by the size of the finite elements, see e.g. [7]. Due to that reason the majority of the analysed cases are simulated with three meshes.

All simulations are performed using novel symbolic-numerical packages of Wolfram Mathematica called AceGen and AceFEM [9]. The former package is a code generator which allows for the implementation of highly nonlinear constitutive models. From this point of view, the most useful capability of AceGen is automatic differentiation which significantly simplifies the process of linearization of equations for the Newton–Raphson procedure. The solution algorithm for the elastoplastic model implemented within AceGen is presented in [28], whereas thermoplasticity is approached in [27]. The latter package, AceFEM, is a finite element software, which thoroughly cooperates with AceGen, and is equipped with a preprocessor, computational engine, and postprocessing tools. Computational tests, for which results are presented in this paper, are carried out using standard eight-noded hexahedral elements with linear interpolation of all unknown fields. To prevent the danger of volumetric locking phenomena the *F-bar* methodology [6] is applied.

At this stage, it is worth highlighting the new aspects of the research, which are presented in this paper. First, the dependence of the unstable response of the rectangular flat membrane in tension to out-of-plane constraints (plane stress vs plane strain conditions) is examined for finite strain plasticity and thermoplasticity. Second, the influence of different parameters of the Burzyński–Drucker–Prager plasticity function on the localized deformation, in particular on the inclination angle of the simulated shear band, is investigated. The special case of zero friction angle, which corresponds to the Huber–Mises–Hencky yield criterion, is also taken into account. Third, the sensitivity of the simulation results to the finite element discretization is examined for hardening, ideal, and softening (thermo)plasticity. Finally, the regularizing effect of conductivity in the thermoplastic material model with thermal and material softening for plane stress and plane strain conditions is assessed.

This paper is laid out as follows. In Section 2, the mathematical formulation of the analysed elastoplastic material model is presented. In Section 3, the description of the implemented benchmark is included. The core part of the paper is in Section 4, which contains the results of the numerical simulations. They are grouped in two subsections: the analysis of the plate in the plane strain and plane stress states. For each case, the influence the of adopted yield function and conductivity is investigated. For selected simulations, the imperfection-dependence is additionally tested. The conclusions are summarized in Section 5.

2. Theory

2.1. *Isothermal model*

2.1.1. *Kinematics*

A deformable continuous body $\mathcal{B}$ with boundary $\partial\mathcal{B}$ is considered. Vector $\mathbf{X}$ denotes the referential location of the body particles at time t_0 and vector $\mathbf{x}(\mathbf{X}, t)$ identifies the current position of particle $\mathbf{X}$ at time t. Function $\mathbf{x} = \boldsymbol{\varphi}(\mathbf{X}, t)$ describes the motion of the body. The deformation gradient and its determinant are defined as usual

$$\mathbf{F} = \frac{\partial \boldsymbol{\supset}(\mathbf{X}, t)}{\partial \mathbf{X}}, \quad J = \det(\mathbf{F}) \tag{2.1}$$

Following [10,11] the deformation gradient can be decomposed into elastic and plastic parts

$$\mathbf{F} = \mathbf{F}^e \mathbf{F}^p \tag{2.2}$$

2.1.2. Free energy functional

The free energy potential per unit volume in the reference configuration, which expresses the state of material, is assumed in the decoupled form:

$$\psi(\mathbf{b}^e, \gamma) = \psi^e(\mathbf{b}^e) + \psi^p(\gamma) \tag{2.3}$$

where the elastic left Cauchy–Green tensor $\mathbf{b}^e$ is defined as

$$\mathbf{b}^e = \mathbf{F}^e(\mathbf{F}^e)^{\mathrm{T}} \tag{2.4}$$

and γ is a plastic strain measure, $\psi^e(\mathbf{b}^e)$ refers to the elastic response and $\psi^p(\gamma)$ denotes the potential of isotropic strain hardening in plasticity.

Based on [20,21,29] the elastic and plastic parts of the free energy potential are defined in the further analysis in the following forms:

$$\psi^e(\mathbf{b}^e) = \frac{1}{2}G\left(\mathrm{tr}(\det(\mathbf{b}^e)^{-1/3}\mathbf{b}^e) - 3\right) + \frac{1}{2}K\ln(J^e)^2 \tag{2.5}$$

$$\psi^p(\gamma) = \frac{1}{2}H\gamma^2 \tag{2.6}$$

where G and K are shear and bulk moduli, respectively, and H is a linear hardening coefficient.

The Kirchhoff stress tensor and hardening function are then respectively derived as follows:

$$\boldsymbol{\tau} = 2\frac{\partial\psi}{\partial\mathbf{b}^e}\mathbf{b}^e, \quad h = \frac{\partial\psi}{\partial\gamma} \tag{2.7}$$

2.1.3. Yield conditions

To complete the constitutive description the yield condition which specifies elastic and plastic regimes is defined

$$F_p(\boldsymbol{\tau}, \gamma) = f(\boldsymbol{\tau}) - \sqrt{2/3}\sigma_y(\gamma) \le 0 \tag{2.8}$$

where $f(\boldsymbol{\tau})$ is a stress measure and $\sigma_y(\gamma)$ is defined as $\sigma_y(\gamma) = \sigma_{y0} + H\gamma$.

Two yield functions, the classical Huber–Mises–Hencky (HMH) and pressure-dependent Burzyński–Drucker–Prager (BDP), are defined as:

$$f_{HMH} = \sqrt{2J_2} \tag{2.9}$$

$$f_{BDP} = \sqrt{2J_2} - \frac{\alpha}{3}I_1 \tag{2.10}$$

where

$$\alpha = \frac{3\tan(\phi)}{\sqrt{9 + 12\tan(\phi)}} \tag{2.11}$$

$$I_1 = \boldsymbol{\tau}_{dev} : \mathbf{I} \tag{2.12}$$

$$J_2 = \frac{1}{2}\cdot\boldsymbol{\tau}_{dev}^2\cdot\mathbf{I} \tag{2.13}$$

ϕ is the friction angle and $\boldsymbol{\tau}_{dev}$ is the deviatoric part of $\boldsymbol{\tau}$.

In particular, the associate flow rule is formulated using the Lie derivative of $\mathbf{b}^e$ following [20]

$$\frac{1}{2}\mathcal{L}_v\mathbf{b}^e = \dot{\lambda}\mathbf{N}\mathbf{b}^e \tag{2.14}$$

where $\mathbf{N}$ denotes the normal to the yield surface and $\dot{\lambda}$ is the plastic multiplier satisfying the standard Kuhn–Tucker conditions:

$$\dot{\lambda} \ge 0, \quad F_p \le 0, \quad \dot{\lambda}F_p = 0 \tag{2.15}$$

For simplicity we further assume that the plastic multiplier plays the role of the plastic strain measure rate $\dot{\gamma} = \dot{\lambda}$

2.2. Thermoplasticity model

2.2.1. Kinematics

For the thermoplastic model, Eq. (2.2) expands to

$$\mathbf{F} = \mathbf{F}^\theta\mathbf{F}^e\mathbf{F}^p = \mathbf{F}^\theta\mathbf{F}^m \tag{2.16}$$

where $\mathbf{F}^m$ denotes the mechanical part of the deformation gradient [18,29]. The thermal contribution $\mathbf{F}^\theta$ is assumed to be purely volumetric, therefore it can be defined in the following way

$$\mathbf{F}^\theta = (J^\theta)^{1/3}\mathbf{I}, \quad J^\theta = \det(\mathbf{F}^\theta) \tag{2.17}$$

where $\mathbf{I}$ is the second order identity tensor and the deformation caused by the temperature change is specified in the following form [13]

$$J^\theta = e^{3\alpha_T(T - T_0)} \tag{2.18}$$

In Eq. (2.18), T is an absolute temperature, T_0 denotes a reference temperature (for a strain-free state), and α_T is the coefficient of linear thermal expansion.

Based on decomposition (2.16) and assumption (2.18), the mechanical part of the deformation gradient can be determined as

$$\mathbf{F}^m = e^{-\alpha_T(T - T_0)}\mathbf{F} \tag{2.19}$$

The illustration of the deformation decomposition can be found in [27].

2.2.2. Free energy functional

For thermoplasticity the free energy potential has the following form

$$\psi(\mathbf{b}^e, T, \gamma) = \psi^e(\mathbf{b}^e) + \psi^\theta(T) + \psi^p(\gamma) \tag{2.20}$$

where

$$\psi^\theta(T) = c\left((T-T_0) - T\cdot\ln\left(\frac{T}{T_0}\right)\right) \tag{2.21}$$

and the first and third components are defined by Eqs. (2.5) and (2.6), respectively.

According to [21], the heat capacity can be defined as $c = -T\frac{\partial^2\psi}{\partial T^2}$. For the adopted form of the free energy capacity c is constant.

2.2.3. *Heat conduction*

The constitutive relation for heat conduction is the classical Fourier law for isotropic materials, which is formulated here using the Kirchhoff heat flux vector $\mathbf{q}$

$$\mathbf{q} = -k\nabla T \tag{2.22}$$

where k is a heat conduction coefficient. The Kirchhoff heat flux is related to the Cauchy heat flux $\mathbf{q}^C$ defined in the current configuration through the formula: $\mathbf{q} = J\mathbf{q}^C$.

2.2.4. *Thermal softening*

The majority of elastic–plastic materials exhibit a reduction in yield strength with a temperature increase. In this paper the yield stress has the following form [27]

$$\sigma_y(\gamma, T) = (\sigma_{y0} + H\gamma)(1 - H_T(T-T_0)) \tag{2.23}$$

where H and H_T are a linear hardening modulus and a thermal softening modulus, respectively. Different formulations of thermal softening and their numerical verification can be found in [26].

2.3. *Governing equations*

Due to the distinction between the reference and the current configurations in large strain analysis, the governing equations can be formulated in the material description, see for example [22], or in the spatial description, for example [21]. In the present model, the spatial quantities are used, however, they are referred to the volume/surface in the reference configuration, see for instance [14].

Two governing equations, which describe the analysed coupled problem, are the balance of linear momentum presented in the local form in Eq. (2.24) and the energy balance written in the temperature form [21] in Eq. (2.25).

$$\rho_0\frac{\partial^2\boldsymbol{\varphi}}{\partial t^2} = J\mathrm{div}(\boldsymbol{\tau}/J) + \rho_0\mathbf{B} \tag{2.24}$$

$$c\frac{\partial T}{\partial t} = J\mathrm{div}(-\mathbf{q}/J) + \mathcal{R} \tag{2.25}$$

In Eq. (2.24), div(·) is the divergence computed with respect to Eulerian coordinates, ρ_0 is the reference density, and $\mathbf{B}$ is a given spatial body force field. For the static analysis, which is presented in this paper, the left–hand side of Eq. (2.24) is equal to zero.

In Eq. (2.25), $\mathcal{R}$ is a heat source density. In the adopted model, it includes heating due to plastic dissipation and has the following form [29]

$$\mathcal{R} = \sqrt{\frac{2}{3}}\chi\sigma_y\dot{\gamma} \tag{2.26}$$

Parameter χ, in Eq. (2.26), denotes a dissipation heat factor which for simplicity is assumed to be constant, cf. [24], but the results of [18] can also be applied.

The balance of linear momentum (2.24) is completed with boundary conditions for displacements $\mathbf{u}$ and tractions $\mathbf{t}$:

$$\begin{aligned}&\mathbf{u} = \hat{u} \quad \text{on} \quad \partial\mathcal{B}_u\\ &\mathbf{t} = \boldsymbol{\tau}\cdot\mathbf{n} = \hat{\mathbf{t}} \quad \text{on} \quad \supset(\partial\mathcal{B}_\tau)\end{aligned} \tag{2.27}$$

where

$$\partial\mathcal{B}_u \cup \partial\mathcal{B}_\tau = \partial\mathcal{B} \quad \text{and} \quad \partial\mathcal{B}_u \cap \partial\mathcal{B}_\tau = \emptyset \tag{2.28}$$

The energy balance equation (2.25) is also complemented with appropriate boundary conditions:

$$\begin{aligned}&T = \tilde{T} \quad \text{on} \quad \partial\mathcal{B}_T\\ &\mathbf{q}\cdot\mathbf{n} = \tilde{q} \quad \text{on} \quad \supset(\partial\mathcal{B}_q)\end{aligned} \tag{2.29}$$

where

$$\partial\mathcal{B}_T \cup \partial\mathcal{B}_q = \partial\mathcal{B} \quad \text{and} \quad \partial\mathcal{B}_T \cap \partial\mathcal{B}_q = \emptyset \tag{2.30}$$

The weak forms of the governing equations are the basis for the finite element implementation. Applying the standard derivation: multiplication by test function $\delta\mathbf{u}$, integration over body $\mathcal{B}$, application of divergence theorem and Neumann boundary conditions, the balance of linear momentum has the following weak form

$$\int_{\mathcal{B}} (\nabla\delta\mathbf{u} : \boldsymbol{\tau} + \delta\mathbf{u}\cdot\mathbf{B})\mathrm{d}V + \int_{\supset(\partial\mathcal{B}_\tau)} \delta\mathbf{u}\cdot\hat{\mathbf{t}}\mathrm{d}a = 0 \tag{2.31}$$

The weak form of the energy balance equation (2.25) is also obtained using the standard procedure and the backward Euler scheme for time integration. The following integral equation, valid for the current time moment is obtained

$$\int_{\mathcal{B}} \left(\delta T\frac{c}{\Delta t}(T-T_n) + \nabla\delta T k\nabla T - \delta T\mathcal{R}\right)\mathrm{d}V + \int_{\supset(\partial\mathcal{B}_q)} \delta T\hat{q}\mathrm{d}a = 0 \tag{2.32}$$

where T_n is the value of temperature at the previous time instant and Δt is the time increment.

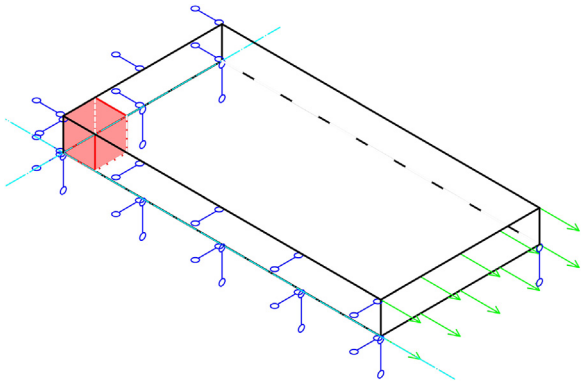

Fig. 1 – The boundary conditions for one-eighth of specimen in plane stress tension (imperfection is marked shaded at the centre). For plane strain, displacement in thickness direction is blocked at every node.

3. Benchmark

All tests shown in this paper have been performed for a rectangular plate in plane strain or plane stress conditions, see Fig. 1. Two different plasticity functions are used and two cases are considered: isothermal and conductive. For the discussion of adiabatic case, refer to [27].

The isothermal model was applied with the HMH and BDP plasticity functions in three different cases: hardening (Hard, $H = 207 \times 10^6$ Pa or $H = 207 \times 10^7$ Pa), ideal plasticity (IP, $H = 0$ Pa), and softening (Soft, only for HMH, $H = -207 \times 10^6$ Pa). Two values of friction angle, 15° and 30°, are used for BDP.

The conductive model is tested with HMH and BDP plasticity, for the latter case, only the 15° friction angle is considered. The softening case is considered with different values of the heat conduction coefficient. The dimensions of the plate are: 0.2 m × 0.1 m × 0.005 m. Due to the symmetry of the sample, only one-eighth of the plate is considered. A cube-shaped imperfection of size 0.005 m is assumed at the center, see Fig. 1. The imperfection is assumed as the decrease of the initial yield stress σ_{y0} and can change. The material parameters are presented in Table 1. The bottom part of the table is related only to the conductive case, whereas the upper part refers to both the isothermal and conductive model. Notice that for the conductive model, thermal softening is always involved.

Three different densities of the finite element mesh are applied: a coarse mesh (called further mesh1, 800 elements, 40 × 20 × 1), see Fig. 2, a medium mesh (called further mesh2, 3200 elements, 80 × 40 × 1), and a fine mesh (called further mesh3, plane strain: 12,800 elements, 160 × 80 × 1 and plane stress: 25,600 elements, 160 × 80 × 2). Mesh3 was considered only for selected cases.

All pictures are presented at the final step of the analysis.

4. Numerical simulations

In this section, the results of numerical simulations are presented. First, the analysis focuses on the isothermal material behaviour with different boundary conditions and then on the HMH or BDP yield function. Then computations are repeated for the model with thermal conductivity.

Loading is applied by extending the specimen in the length direction with the maximum displacement equal to 0.08 m, multiplied by $\lambda \in [0, 1]$. The sum of reactions in every convergent load step is monitored. The total time of deformation is one second.

4.1. *Plane strain*

4.1.1. *Isothermal, HMH*

Firstly, simulations for plane strain and isothermal conditions for HMH plasticity are presented. The diagram of the sum of reactions vs the load multiplier is shown in Fig. 3. No mesh sensitivity is observed for the hardening case ($H = 207 \times 10^6$ Pa) and small dependence is visible for ideal plasticity ($H = 0$ Pa). It can be noted that the response for mesh1 is stiffer than that for the finer meshes, and strong mesh–sensitivity occurs for softening ($H = -207 \times 10^6$). The deformed meshes with plots of accumulated plastic strain measure at the end of the deformation process are shown in Fig. 4. Although small softening is observed for plasticity with hardening, a uniform deformation mode (notice small differences in equivalent plastic strain) is obtained, see Fig. 4 (left top). For ideal

Table 1 – Material parameters.

Property	Symbol	Value	Unit
Young modulus	E	207×10^9	N/m^2
Poisson ratio	ν	0.29	–
Yield threshold in tension	σ_{y0}	450×10^6	N/m^2
Linear hardening modulus	H	$-207 \times 10^6/0/207 \times 10^6/207 \times 10^7$	N/m^2
Angle of friction	ϕ	15/30	deg
Density	ρ	24×10^3	kg/m^3
Conductivity	k	100/200/300	J/(s K m)
Heat capacity	c	460	J/(kg K)
Thermal expansion coefficient	α_T	12×10^{-6}	1/K
Thermal softening modulus	H_T	0.02	1/K
Dissipation heat factor	χ	0.9	–
Reference temperature	T_0	273.15	K

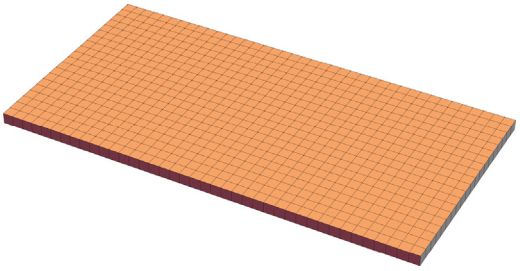

Fig. 2 – Finite element discretization of one-eighth of specimen in tension, coarse mesh (mesh1).

plasticity, the localization has the form of necking, see Fig. 4 (left bottom). On the right-hand side of Fig. 4, two tests for softening are presented for different sizes of load steps. Due to instabilities in computations, unexpected patterns of shear bands (reflected bands) are obtained for the case with larger load steps. Another example is shown in Fig. 5. The same test is computed with different load step sizes. Although the obtained necking patterns are qualitatively similar (mirror reflection), the selection of the load step is a crucial aspect of simulations, hence for large load steps, out-of-balance states during Newton–Raphson iterations can cause localization to occur at a place different than imperfection could suggest. The solution obtained in such localization simulations is not unique. In fact, the energetically preferable mode would involve only one shear band, but other modes can be obtained for longer load steps and/or coarser discretization.

4.1.2. *Isothermal, BDP*

The simulations shown in the previous section are now repeated for BDP plasticity. Two different values of the friction angle: 15° and 30° and two cases: hardening ($H = 207 \times 10^6$ Pa) and ideal plasticity are considered. The results of the numerical computations are shown in Fig. 6. It can be noted that for 15°, we obtain a stiffer response than for 30°, as the increase of friction angle reduces the load-carrying capability. The larger friction angle also causes computational problems which manifest themselves in a faster termination of the simulation. These two phenomena are presented in Fig. 6: for 15° we have the sum of reactions higher and equal to 54,000 N at the peak and the maximum value of λ is equal to 1.0, contrary to the analysis performed for 30° where we have less than the reaction force of 49,500 N at the peak and the maximum value of λ is approximately 0.5. In Fig. 7, the deformation and equivalent plastic strain maps are compared for the final step of analysis with different friction angles. The pattern for 15° can be described as diffuse with a necking shape. The results for 30° (for this case the simulations stops just after the peak) show that the maximum value of

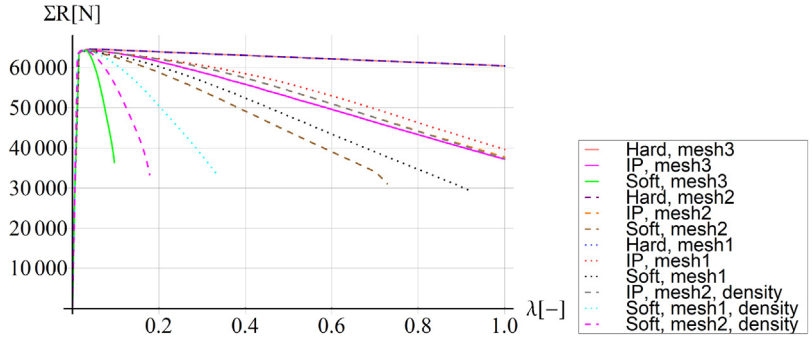

Fig. 3 – Sum of reactions vs displacement multiplier for isothermal, plane strain conditions with HMH plasticity, and imperfection 1% of σ_{y0} (in the legend, IP denotes ideal plasticity, the remark "density" marks smaller load steps).

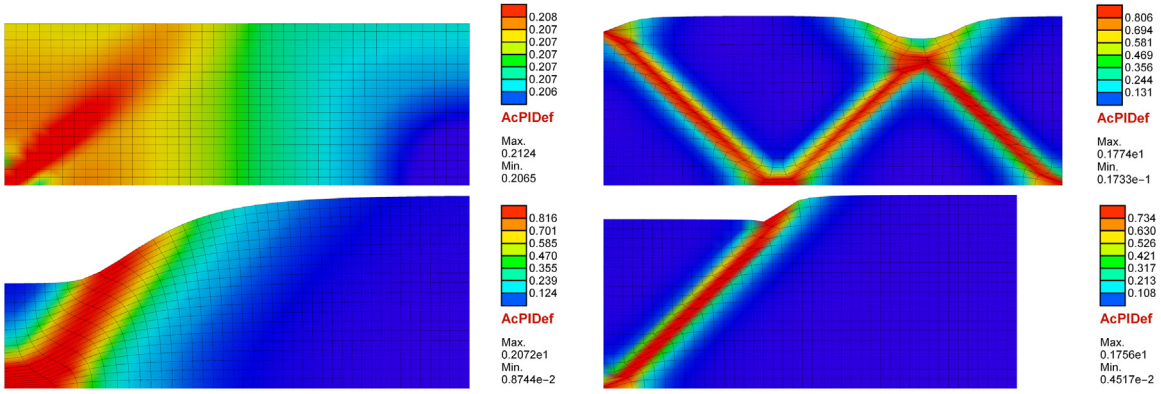

Fig. 4 – Deformed mesh (mesh1) for isothermal, plane strain conditions with HMH plasticity in cases: hardening (left top, $H = 207 \times 10^6$ Pa), ideal plasticity (left bottom, $H = 0$ Pa), softening (right top, $H = -207 \times 10^6$ Pa) and softening with smaller load steps (right bottom). Pictures are presented at final step of the analysis.

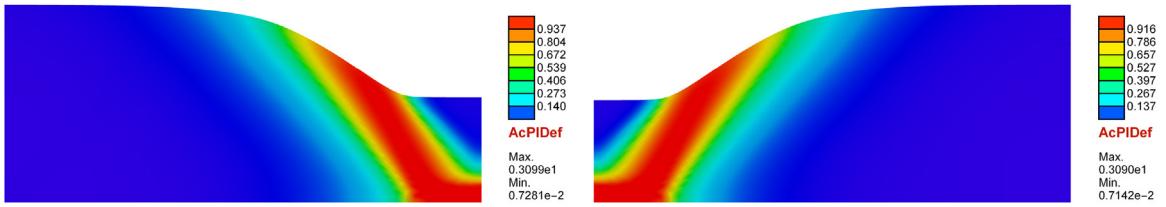

Fig. 5 – Deformed mesh (mesh2) for isothermal, plane strain model with HMH plasticity in cases: ideal plasticity (left) and ideal plasticity with smaller load steps (right).

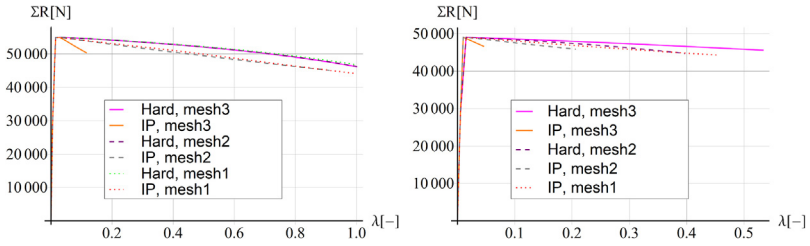

Fig. 6 – Sum of reactions vs displacement multiplier for isothermal, plane strain conditions with BDP plasticity and 1% imperfection for cases $\phi = 15^\circ$ (left), $\phi = 30^\circ$ (right).

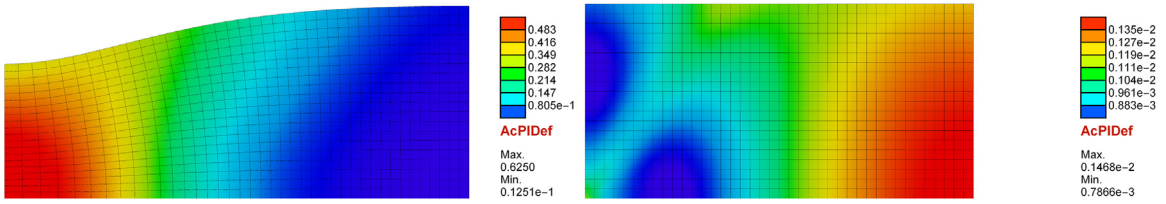

Fig. 7 – Deformed mesh (mesh1) for isothermal, hardening ($H = 207 \times 10^6$ Pa), plane strain conditions with BDP plasticity for cases $\phi = 15^\circ$ (left) and $\phi = 30^\circ$ (right).

accumulated plastic strain is obtained on the opposite side than the imperfection.

The small difference between the onset of plastic regime, shown in Fig. 6 (right), is caused by load steps that are too large in the elastic part of the process. Although a larger number of steps should resolve this problem, it also increases the computation time.

The inclination of the band for models with different friction angles is also analysed. The angles are measured in the undeformed configuration for the same value of $\lambda = 0.21$. For the isothermal plane strain model, the results are 47° (for friction angle 0°), 51° (for friction angle 15°), 55° (for friction angle 30°). Therefore, a correlation between the friction angle and the inclination of the band can be noticed.

4.1.3. *Conductive, HMH*

In this section, the conductive model in plane strain conditions with HMH plasticity is discussed. Three different aspects are varied in the study: imperfection (5% and 20% of σ_{y0}), conductivity (100, 200 and 300 J/(s K m)), and mesh density (mesh1, mesh2 and mesh3, where mesh3 is considered only for the 20% imperfection).

The results for the tests with the two imperfections are presented in Figs. 8 and 9. After analysing the differences between the diagrams, it can be deduced that the imperfection magnitude does not have a significant impact on the computation results. All hardening tests for mesh1, mesh2 and mesh3 coincide, up to a certain point, in the post-peak regime, namely until $\lambda = 0.42$. On the contrary, for softening and ideal plasticity, the diagrams become distinct immediately after reaching the peak. Small mesh sensitivity can be observed for all tests because of the regularizing influence of conduction, although two softening sources, material (negative value of H) and thermal, are used. The lower value of conductivity and finer mesh cause a less ductile response of the material (see Fig. 10). As shown in Fig. 10, the diagrams obtained for mesh1 for different conductivities are closer to each other than the diagrams for the same conductivity and

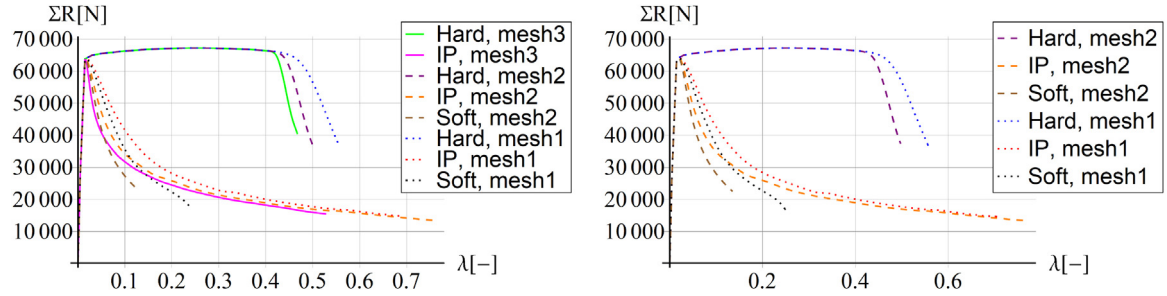

Fig. 8 – Sum of reactions vs displacement multiplier for conductive (k = 100 J/(s K m)), plane strain conditions with HMH plasticity, 20% of σ_{y0} imperfection (left) and 5% of σ_{y0} imperfection (right). Hardening modulus for hardening case is equal to 207×10^7 Pa (1% of E).

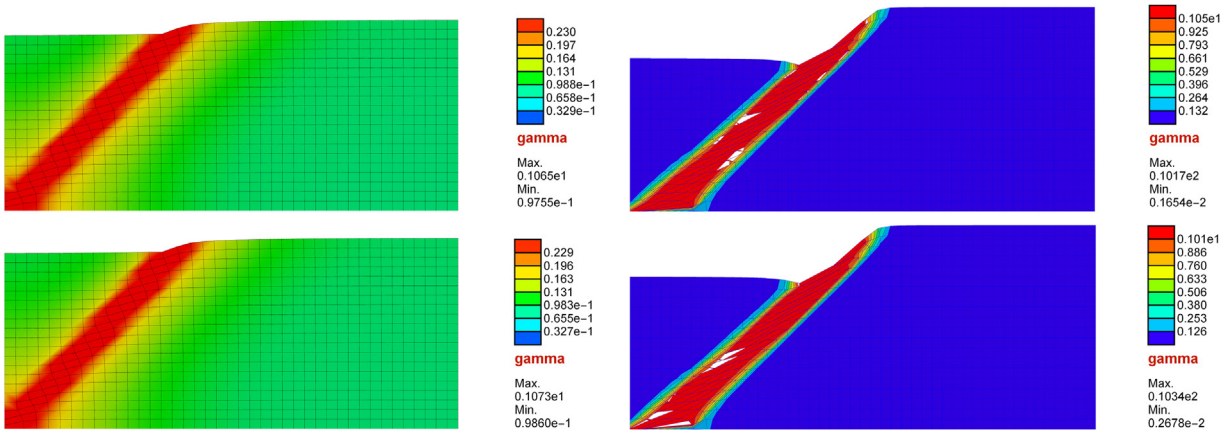

Fig. 9 – Deformed mesh (mesh1) for conductive, plane strain conditions with HMH plasticity, k = 100 J/(s K m), and four different cases: hardening ($H = 207 \times 10^6$ Pa) with 20% of σ_{y0} imperfection (left top), hardening ($H = 207 \times 10^6$ Pa) with 5% of σ_{y0} imperfection (left bottom), ideal plasticity with 20% of σ_{y0} imperfection (right top), ideal plasticity with 5% of σ_{y0} imperfection (right bottom).

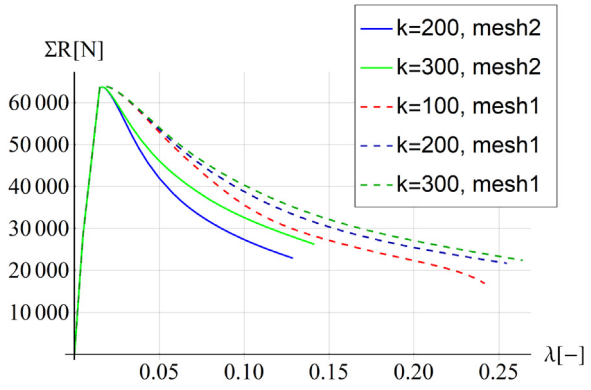

Fig. 10 – Sum of reactions vs displacement multiplier for conductive, plane strain conditions with HMH plasticity, material and thermal softening, and different conductivity Diff id="33">[33_TD$DIFF] coefficients, imperfection is 20% of σ_{y0} and $H = -207 \times 10^6$ Pa.

for different meshes. The diagrams for mesh1 coincide to point $\lambda = 0.03$ and for mesh2 to point $\lambda = 0.02$. It can also be noticed that for all values of conductivity we obtain a similar shear band rather than necking (see Fig. 11).

4.1.4. *Conductive, BDP*

Similar to isothermal computations, the previous tests for HMH are now repeated for BDP plasticity, but only for the friction angle of 15°. Unfortunately, the simulations end at the beginning of the process (see Figs. 12 and 13). Note that the computations stop when λ reaches 0.06, or even less. No imperfection sensitivity can be observed for hardening (the left part of Fig. 12). For ideal plasticity (the right part of Fig. 12) and hardening, mesh–sensitivity is visible. In Fig. 12, only one test for 5% imperfection is presented because of a premature termination of computations. It is the main reason why a stronger imperfection is considered in a part of computations (this results in more stable calculations).

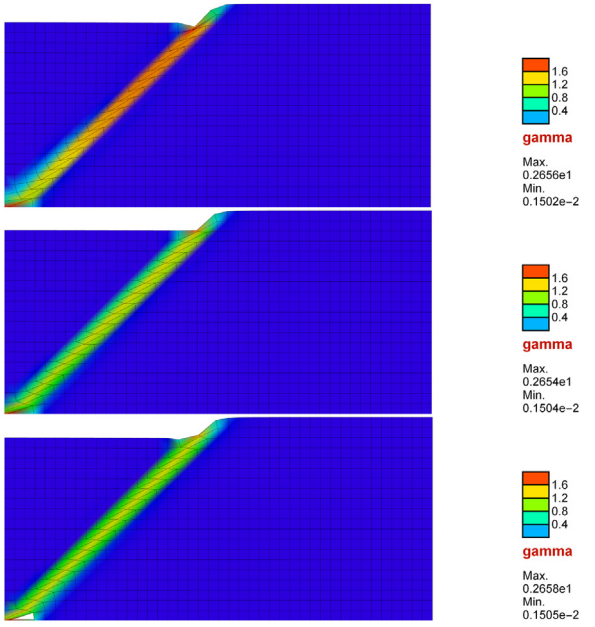

Fig. 11 – Deformed mesh (mesh1) for conductive, plane strain model with HMH plasticity and material and thermal softening for cases: k = 100 (top), k = 200 (middle) and k = 300 (bottom), $H = -207 \times 10^6$ Pa.

4.2. *Plane stress*

4.2.1. *Isothermal, HMH*

The following sections present isothermal tests for plane stress with HMH plasticity. The imperfection in all cases is 10% of σ_{y0}. The calculation results for $H = 207 \times 10^6$ Pa for hardening and for $H = -207 \times 10^6$ Pa for softening are shown in Fig. 14. Strong mesh sensitivity is visible for all cases; however, the hardening diagrams are distinct only from point $\lambda = 0.14$. As expected, coarser meshes give a more ductile (stiffer) response. The diagrams presented in Fig. 14 are associated with a localized mode of deformation. This is confirmed in Fig. 15, in which shear bands are presented. In the presence of geometrical softening, material hardening can be insufficient to prevent mesh–sensitivity.

4.2.2. *Isothermal, BDP*

The simulations from the previous section are repeated with the BDP yield function. The problems that occurred previously for models with BDP plasticity are also visible in the current tests. The computations end at the beginning of the process and certain mesh sensitivity is presented in Fig. 16. The stiffer response for the coarser meshes can be observed. The deformed meshes with plastic strain distributions at the end of the deformation process are shown in Fig. 17. However, because of the above-mentioned problems with continuation of computation, the beginning of the shear band formation can be observed. For example, the simulations for hardening case end for mesh1 when $\lambda = 0.26$, for mesh2 when $\lambda = 0.16$, and for mesh3 when $\lambda = 0.15$. A wider deformation zone can be observed for tests with increasing value of hardening modulus (i.e. hardening, ideal plasticity and softening).

The inclination of the localization band for models with different friction angles is also analysed. The angles are measured in the undeformed configuration for the same value of $\lambda = 0.06$. For the isothermal plain stress model, the inclinations are equal to 56° (for friction angle 0°), 60° (for friction angle 15°) and 64° (for friction angle 30°). Therefore, a correlation can be noticed between the friction angle and the inclination of the band.

4.2.3. *Conductive, HMH*

The next simulations are performed for conductive, plane stress case, assuming the HMH plasticity and 10% imperfection. Similar to the plane strain tests with conductivity and the HMH yield function, the results of the test with hardening for mesh1, mesh2, and mesh3 coincide up to the point $\lambda = 0.35$ and then differ (see Fig. 18). In Fig. 19, the deformed mesh with the distribution of accumulated plastic strain is depicted. The distinct shear band is visible for ideal-plasticity and softening. However, because of a fast disruption of calculations due to rapid reduction of stiffness, only the beginning of the shear band formation process can be seen for hardening.

4.2.4. *Conductive, BDP*

The last simulations presented in this paper are computed for a conductive, plane stress model with the BDP plasticity. The difference between the peak position, similar to Fig. 6, occurs in Fig. 20. As was written, applying a larger number of load steps should resolve the problem. The mesh sensitivity is visible only for ideal plasticity; however, we can see the results obtained for the model with strain hardening only for mesh1 and mesh2, due to the fact that the calculations for mesh3 diverge at the beginning of the plastic process. The plastic strain distribution with the deformed mesh at the end of the deformation process is presented in Fig. 21.

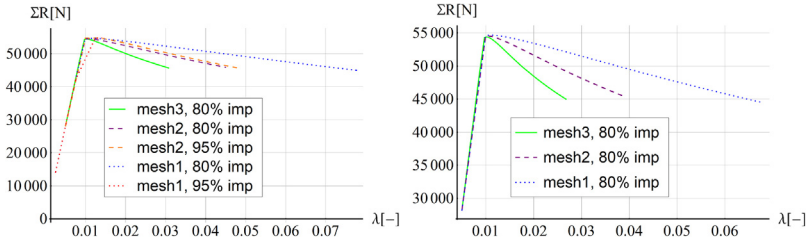

Fig. 12 – Sum of reactions vs displacement multiplier for conductive, plane strain conditions with BDP plasticity for k = 100 J/(s K m) and ϕ = 15 in two cases: hardening (left, $H = 207 \times 10^6$ Pa) and ideal plasticity (right).

Fig. 13 – Deformed mesh (mesh1) for conductive, plane strain conditions with BDP plasticity, imperfection 20% of σ_{y0}, $\phi = 15^{\circ}$, $k = 100$ J/(s K m), ideal plasticity.

5. Conclusions

This paper presents a parametric study of localized deformation for large strain plasticity with and without thermo-mechanical coupling. In particular, the calculations consider the two yield functions (Huber–Mises–Hencky and Burzyński–Drucker–Prager), different values of hardening modulus, conductivity, and friction angle. Three discretizations are employed for the majority of tests.

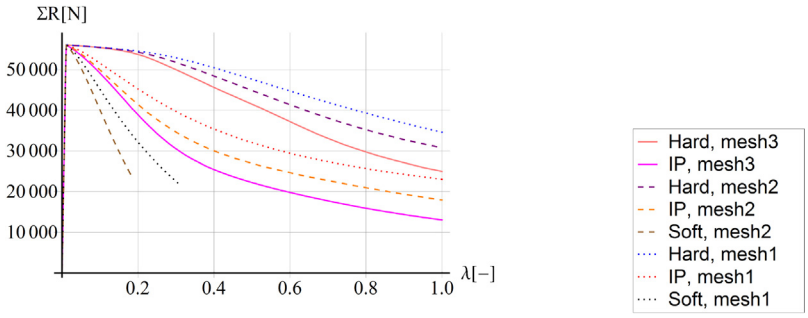

Fig. 14 – Sum of reactions vs displacement multiplier for isothermal, plane stress conditions with HMH plasticity, and imperfection 10% of σ_{y0}.

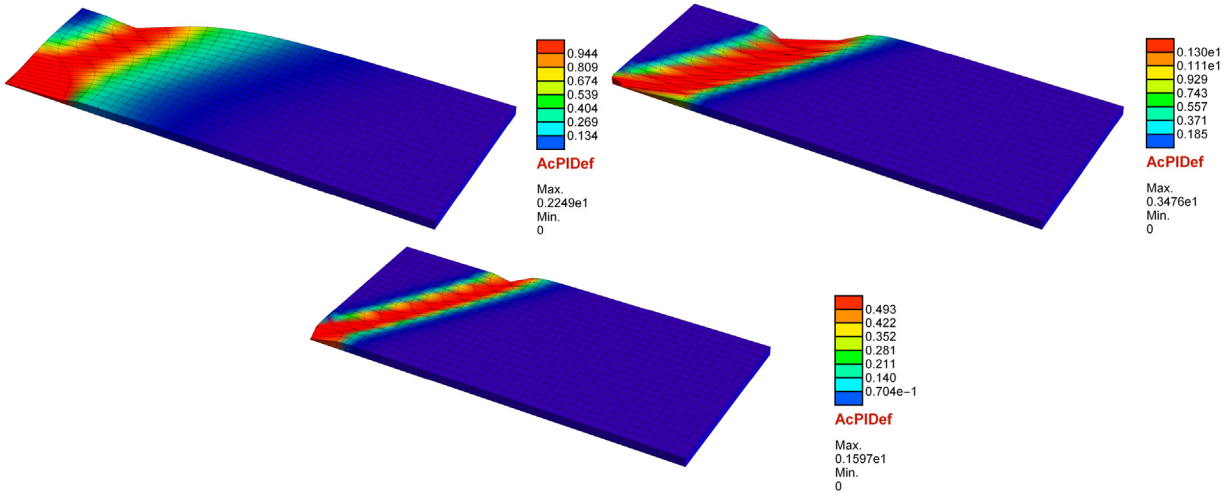

Fig. 15 – Deformed mesh (mesh1) for isothermal, plane stress conditions with HMH plasticity in cases: hardening (left top, $H = 207 \times 10^6$ Pa), ideal plasticity (right top) and softening (bottom, $H = -207 \times 10^6$ Pa).

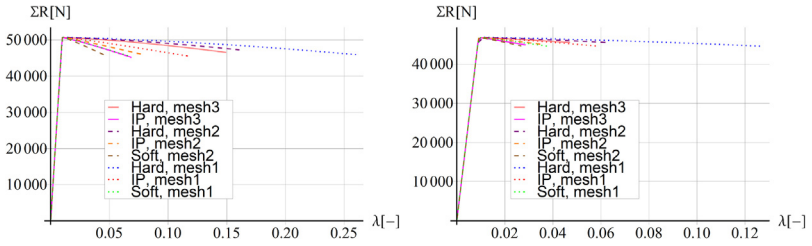

Fig. 16 – Sum of reactions vs displacement multiplier for isothermal, plane stress conditions with BDP plasticity, 10% imperfection , friction angle 15° (left) and for 30° (right).

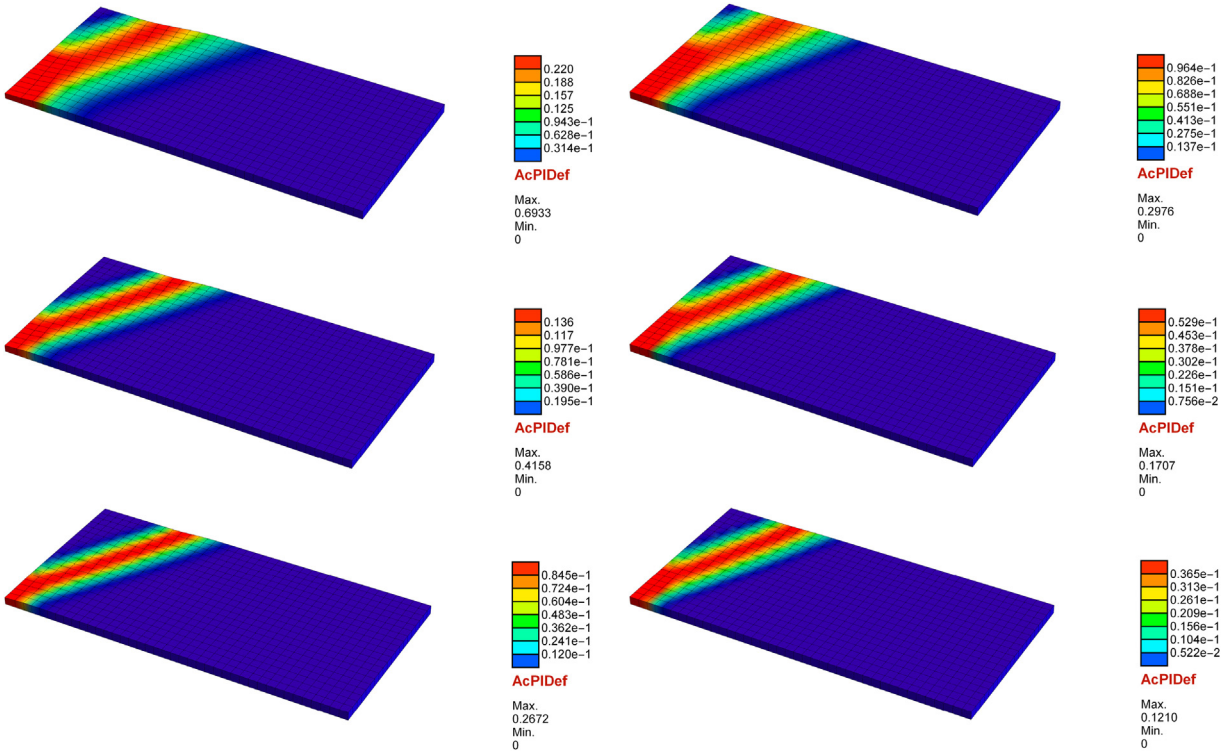

Fig. 17 – Deformed mesh (mesh1) for isothermal, plane stress conditions with BDP plasticity: on the left for $\phi = 15^\circ$, on the right for $\phi = 30^\circ$, and three cases: hardening (top, $H = 207 \times 10^6$ Pa), ideal plasticity (middle), softening (bottom, $H = -207 \times 10^6$ Pa).

For the isothermal, plane strain model, no mesh sensitivity can be observed for hardening, small mesh sensitivity for ideal plasticity, and strong mesh sensitivity for softening. In plane stress regime, mesh sensitivity is visible for all cases. The addition of the strain constraint in the thickness direction causes a more stable behaviour of the specimen. The thickness of the plate in a shear band is reduced in the plane stress model.

From the computational point of view, the behaviour of a material modelled with the HMH yield function is more stable,

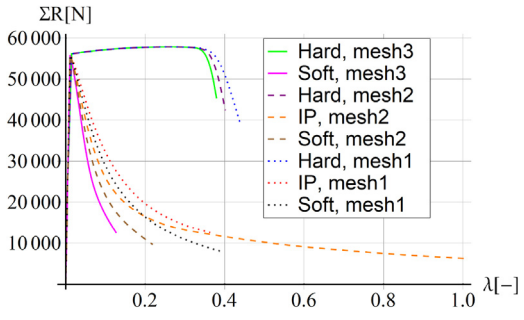

Fig. 18 – Sum of reactions vs displacement multiplier for conductive, plane stress conditions with HMH plasticity, imperfection 20% of σ_{y0} and $k = 100$ J/(s K m). Hardening modulus for hardening case is $H = 207 \times 10^7$ Pa (1% of E) and for softening $H = -207 \times 10^6$ Pa (−0.1% of E).

computations continue to the end of the assumed loading process, and the imperfection magnitude does not influence the results significantly. In contrast to HMH, the use of the BDP yield function leads to computational problems. The process often ends just after the onset of the plastic yielding, especially for ideal plasticity and softening cases. The possible cause for the divergence in computation is that the BDP surface in stress space has a vertex, at which the normal **N**cannot be computed uniquely. Due to that fact, problems with convergence occur. The solution to this problem can be the application of the Hoffman yield function, for which the vertex is smoothed. In selected cases, a stronger imperfection prevents the computations from the quick divergence. For this reason, the simulations of the thermomechanical models are performed with 20% of σ_y imperfection.

However, the numerical tests performed for the isothermal model have been repeated using the thermomechanical description. In the analysed cases, heat conduction does not regularize the response sufficiently. It can be a result of the presence of two types of softening: material and thermal. The thermal softening effect is strong enough to cause a quick loss of stiffness, and consequently, terminate the computation.

The inclination of the band for isothermal, plane stress and plain strain models with different friction angles has also been analysed. In both cases a correlation between the friction angle and the inclination of the band can be noticed. Although the inclinations are larger for the plane strain case, the differences between the models with friction angles 0°, 15°, and 30° are similar and equal to around 4°.

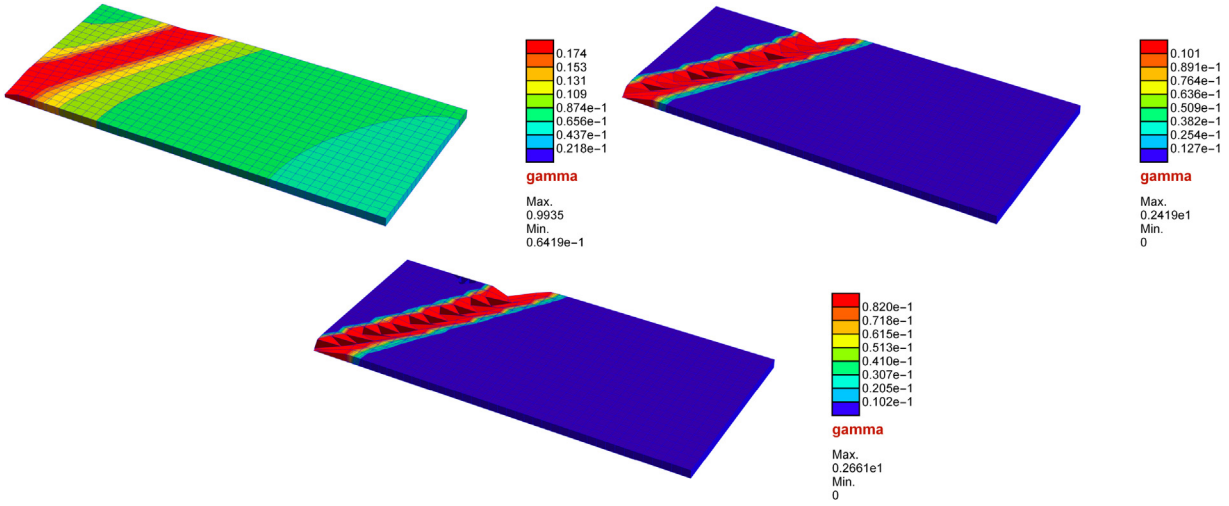

Fig. 19 – Deformed mesh (mesh1) for conductive, plane stress conditions with HMH plasticity: hardening (left top, $H = 207 \times 10^7$ Pa), ideal plasticity (right top) and softening (bottom, $H = -207 \times 10^6$ Pa).

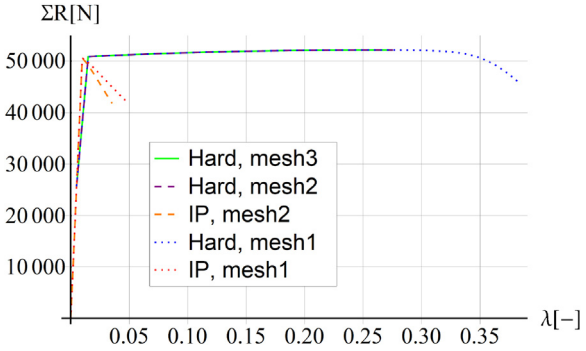

Fig. 20 – Sum of reactions vs displacement multiplier for conductive, plane stress conditions with BDP plasticity and imperfection 20% of σ_{y0} and $k = 100$ J/(s K m). The hardening modulus for hardening is $H = 207 \times 10^7$ Pa (1% of E) and for softening $H = -207 \times 10^6$ Pa (−0.1% of E).

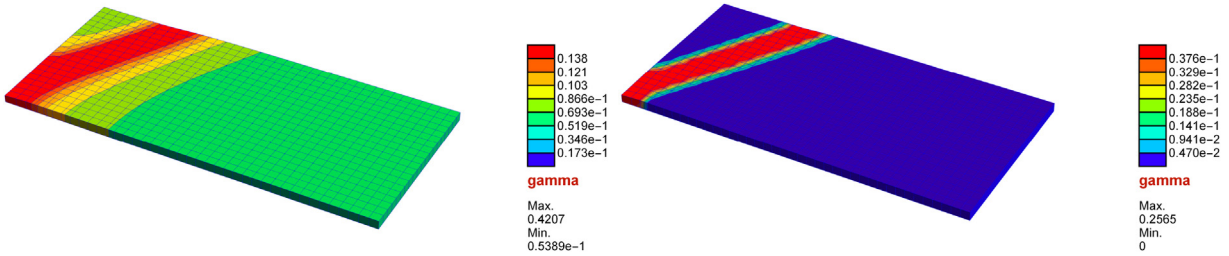

Fig. 21 – Deformed mesh (mesh1) for conductive, plane stress conditions with BDP plasticity in cases hardening (left, $H = 207 \times 10^7$ Pa), ideal plasticity (right).

REFERENCES

[1] F. Aldakheel, C. Miehe, Coupled thermomechanical response of gradient plasticity, Int. J. Plast. 91 (2017) 1–24.

[2] R.C. Batra, C.H. Kim, Effect of thermal conductivity on the initiation, growth and bandwidth of adiabatic shear bands, Int. J. Eng. Sci. 29 (8) (1991) 949–960.

[3] A. Benallal, D. Bigoni, Effects on temperature and thermo-mechanical couplings on material instabilities and strain localization of inelastic materials, J. Mech. Phys. Solids 52 (2004) 725–753.

[4] D. Bigoni, Nonlinear Solid Mechanics: Bifurcation Theory and Material Instability, Cambridge University Press, Cambridge, 2012.

[5] R. de Borst, L.J. Sluys, H.-B. Mühlhaus, J. Pamin, Fundamental issues in finite element analyses of localization of deformation, Eng. Comput. 10 (1993) 99–121.

[6] E.A. de Souza Neto, D. Peric, D.R.J. Owen, Computational Methods for Plasticity: Theory and Applications, John Wiley & Sons, Ltd., Chichester, UK, 2008.

[7] S. Forest, E. Lorentz, Localization phenomena and regularization methods, in: J. Besson (Ed.), Local Approach to Fracture, Les Presses de l'École des Mines, Paris, 2004 311–370.

[8] R. Hill, A general theory of uniqueness and stability in elastic–plastic solids, J. Mech. Phys. Solids 6 (1958) 236–249.

[9] J. Korelc, Automation of primal and sensitivity analysis of transient coupled problems, Comput. Mech. 44 (2009) 631–649.

[10] E.H. Lee, Elastic plastic deformation at finite strain, ASME Trans. J. Appl. Mech. 36 (1969) 1–6.

[11] E.H. Lee, D.T. Liu, Finite-strain elastic–plastic theory with application to plane-wave analysis, J. Appl. Phys. 38 (1967) 19–27.

[12] J. LeMonds, A. Needleman, Finite element analyses of shear localization in rate and temperature dependent solids, Mech. Mater. 5 (1986) 339–361.

[13] S.C.H. Lu, K.S. Pister, Decomposition of deformation and representation of the free energy function for isotropic thermoelastic solids, Int. J. Solids Struct. 11 (1975) 927–934.

[14] C. Miehe, Entropic thermoelasticity at finite strains. Aspects of the formulation and numerical implementation, Comput. Methods Appl. Mech. Eng. 120 (1995) 243–269.

[15] L.P. Mikkelsen, Necking in rectangular tensile bars approximated by a 2-D gradient dependent plasticity model, Eur. J. Mech. A/Solids 18 (5) (1999) 805–818.

[16] S. Okazawa, Structural bifurcation for ductile necking localization, Int. J. Nonlinear Mech. 45 (2009) 35–41.

[17] H. Petryk, Theory of material instability in incrementally nonlinear plasticity, in: H. Petryk (Ed.), Material Instabilities in Elastic and Plastic Solids, Springer-Verlag, Wien/New York, 2000, 261–331, CISM Course Lecture Notes No. 414.

[18] M. Ristinmaa, M. Wallin, N.S. Ottosen, Thermodynamic format and heat generation of isotropic hardening plasticity, Acta Mech. 194 (2007) 103–121.

[19] J.W. Rudnicki, J.R. Rice, Conditions for the localization of deformation in pressure-sensitive dilatant materials, J. Mech. Phys. Solids 23 (1975) 371–394.

[20] J.C. Simo, A framework for finite strain elastoplasticity based on maximum plastic dissipation and the multiplicative decomposition: Part 1. Continuum formulation, Comput. Methods Appl. Mech. Eng. 66 (1988) 199–219.

[21] J.C. Simo, C. Miehe, Associative coupled thermoplasticity at finite strains: formulation, numerical analysis and implementation, Comput. Methods Appl. Mech. Eng. 98 (1992) 41–104.

[22] J.C. Simo, Numerical analysis and simulation of plasticity, in: P.G. Ciarlet, J.L. Lions (Eds.), Handbook of Numerical Analysis. Numerical Methods for Solids (Part 3), vol. VI, Elsevier Science, Boca Raton, 1998 183–499.

[23] S. Stören, J.R. Rice, Localized necking in thin sheets, J. Mech. Phys. Solids 23 (1975) 421–441.

[24] G.I. Taylor, H. Quinney, The latent energy remaining in a metal after cold working, Proc. R. Soc. Lond. Ser. A 143 (1934) 307–326.

[25] V. Tvergaard, Tensile instabilities at large strains, in: Q.S. Nguyen (Ed.), Bifurcation and Stability of Dissipative Systems, Springer-Verlag, Wien/New York, 1993, 251–291, CISM Courses and Lectures No. 327.

[26] B. Wcisło, Simulations of thermal softening in large strain thermoplasticity with degradation, Eng. Trans. 4 (64) (2016) 563–572.

[27] B. Wcisło, J. Pamin, Local and non-local thermomechanical modeling of elastic–plastic materials undergoing large strains, Int. J. Numer. Methods Eng. 109 (1) (2017) 102–124.

[28] B. Wcisło, J. Pamin, K. Kowalczyk-Gajewska, Gradient-enhanced damage model for large deformations of elastic–plastic materials, Arch. Mech. 65 (5) (2013) 407–428.

[29] P.A. Wriggers, C. Miehe, M. Kleiber, J.C. Simo, On the coupled thermomechnical treatment of necking problems via finite element methods, Int. J. Numer. Methods Eng. 33 (1992) 869–883.